COMPUTATIONAL ANALYSIS OF BUBBLE MICRO-LAYER IN SUB-COOLED BOILING

Eyitayo James Owoeye and DuWayne Schubring
Department of Mechanical and Aerospace Engineering, University of Florida
205 Nuclear Science Building, P.O. Box 116300, Gainesville FL 32611-6300, USA
msgenius10@ufl.edu and dlschubring@ufl.edu

ABSTRACT

In sub-cooled flow boiling, bubbles nucleate along the wall, grow rapidly, and then detach from the nucleation site. The growth rate of the bubble (and local heat transfer coefficient) is greatly enhanced by the presence of a micro-layer. This region contains a liquid film that transfers the conducted heat from the wall to the liquid-vapor interface. The thickness of the liquid microlayer affects bubble growth rate as it slides along the wall. The shape of the liquid-vapor interface is determined by a balance of forces due to liquid drag, interface curvature, hydrostatic head, and disjoining pressure. Although most of the heat from the high heat flux is utilized in evaporation through the film later on the nucleation site, this phenomenon is still not yet fully understood. Due to the small spatial scale of the micro-layer relative to the bubble diameter and domain size, computational analysis has proven particularly challenging. In the present work, the unsteady mass, momentum, and energy equations for the microlayer region are solved. The model describes the liquid flow in an evaporating interface of a vapor formed during sub-cooled boiling. The equations are coupled with interface curvature and pressure phase equations to obtain a fourth-order nonlinear ordinary differential (ODE) equation of the micro-layer thickness. The analysis was implemented in MATLAB by using the 4th-order Runge Kutta method. The model is applied to the case of boiling of high-pressure water into steam, of particular relevance to the nuclear industry (LWR applications). It is also of relevance to other high-pressure boiling applications, such as conventional power plants. The effects of varying the wall heat flux and system pressure on the micro-layer thickness and time evolution are also analyzed for the steam-water case.

KEYWORDS
Micro-layer, Sub-cooled boiling, Runge Kutta methods, MATLAB

1. INTRODUCTION

When a bubble is nucleated on a wall, a thin liquid microlayer with thickness of O(10 μm) is present under it [1]. The bubble growth and local heat transfer coefficient is enhanced by the microlayer. This however, results in the diminishing of the microlayer thickness due to evaporation. Eventually, a dry surface area is formed around the nucleation site and the radius of this dry spot gradually increases with time. The bubble microlayer has a significant contribution to the growth rate of a vapor bubble. Analysis of the microlayer at high pressure, high heat flux conditions will improve the prediction of the bubble growth rate as it slides along a heated wall in a nuclear reactor.

Fig. 1 illustrates the microlayer beneath the bubble. θ_1 is the traditional contact angle in the macro region while θ_2 is the micro-contact angle. Fig. 1 also shows the dry spot radius r_d, bubble root radius

R_b, and microlayer thickness δ as a function of radius r and time t.
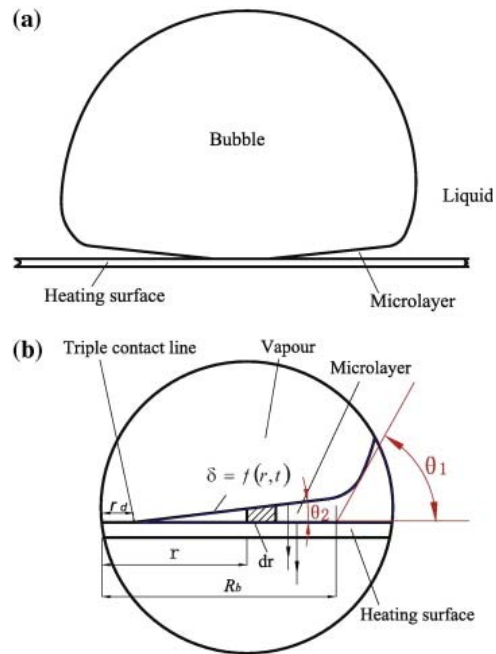
Figure 1: Schematics of the microlayer beneath a bubble [2]

The bubble microlayer has attracted significant research interest due to its importance to bubble growth. Jawurek [3] studied the details of microlayer geometry and bubble growth in a cylindrical boiling tank using high speed interferometric photography. It was reported that the microlayers were wedge-shaped in cross-section for all cases. The result also indicated that microlayers of bubbles with zero waiting time suffered disturbances ranging from mild fringe distortion to total fragmentation.

Li et al. [4] employed reflectance-based fiber-optic laser technique to measure the thickness of the liquid microlayer between a cap-shaped sliding bubble and an inclined heated wall. Millimeter-sized spherical bubbles of FC-87 vapor were injected near the lower end of a uniformly heated aluminum plate. The heated surface was inclined at angles of $2 - 15^o$ from the horizontal. The experiment was done with bulk temperature of 25^oC and at atmospheric pressure. It was reported that the microlayer thickness ranged between $22 - 55$ μm for the cap-shaped bubbles. Their results also indicate that the microlayer thickness is independent of bubble dimension. However, the average microlayer thickness decreased with increasing inclination angle.

Utaka et al. [5] investigated the effects of gap size, velocity of the vapor bubble forefront, and distance from the incipient bubble site on the microlayer thickness in a narrow gap mini/micro-channel boiling system. The variation of microlayer thickness relative to the bubble forefront was divided into two regions. The microlayer thickness increased linearly with increasing velocity on the low velocity region, and constant other regions. The initial microlayer thickness decreased with lower channel gap size, and increased with higher heat flux. It was also verified that heat transfer to the bubble was enhanced by microlayer evaporation.

Utaka et al. [6] experimentally studied that structure of the microlayer that forms between a growing isolated bubble and the heated wall for nucleate pool boiling. Using a measurement system that employs laser extinction method, the microlayer thickness for water and ethanol were measured at

atmospheric pressure. Their result show that the initial microlayer thickness increased linearly with increasing distance from the bubble initiation site. It however decreased with time due to evaporation until the film thickness became zero and a dry region appeared. The reported initial microlayer thickness was approx. $0-9~\mu$m for water and twice as thick for ethanol. The heat flow also had little effect on the initial microlayer thickness for both fluids.

Gao et al. [2] applied a laser interferometric method to study the dynamic characteristics of the microlayer beneath an ethanol vapor bubble during nucleation. Different correlation constants were determined to predict the time variation of dry spot radius and microlayer thickness before a dry spot appears. The authors also reported that microlayer volume increased with time before the dry spot appeared, but decreased afterwards due to evaporation of the microlayer.

Cooper and Lloyd [7] applied a simplified hydrodynamic theory to predict the thickness of a microlayer in term of bubble growth time. A ±15% agreement with experimental data was obtained when their model was applied to the bubble growth rate.

Van Stralen et al. [1] employed Pohlhausen's equation to predict the initial thickness of the evaporative microlayer beneath a hemispherical vapor bubble on a superheated horizontal wall. The Pohlhausen's solution is based on a simplified Navier-Stokes equation without pressure gradient in combination with continuity and heat conduction. The model combined the effects of relaxation microlayer around the bubble dome and evaporation microlayer.

Zhao et al. [8] proposed a theoretical dynamic microlayer model to predict the heat flux in a fully developed nucleate boiling region on horizontal surfaces that includes critical heat flux (CHF). By assuming that heat transfer is mainly due to the evaporation of the microlayer, the microlayer thickness, dryout area, and heat flux were modeled as a function of superheat.

Dhir and colleagues ([9] & [10]) developed a model and numerically solved the shape of the microlayer underneath a bubble by applying lubrication theory. The radial variation in microlayer thickness was governed by capillary pressure, recoil pressure, disjoining pressure, and viscous stresses, while the evaporative heat flux across the liquid-vapor interface was computed using the modified Clausius-Clapeyron equation. A fourth-order ODE was derived for the microlayer thickness by combining the mass, momentum, and energy equations. Christopher and Zhang [11] also modeled the microlayer thickness by applying this model, neglecting the recoil pressure term and using modified boundary conditions. They compared the microlayer heat flux with predictions made by solving the 2-D Navier-Stokes equation in the microlayer under steady state. Their result indicates that the total heat transfer rates across the microlayer increase with bubble size but the increase was not near as fast as the increase in the microlayer interfacial surface area.

Previous numerical works have focused on steady state analysis of the microlayer. The dynamic behavior of microlayer as the bubble slides along the surface is studied in this work. Both the steady and unsteady state behavior of the bubble microlayer thickness was modeled by combining the mass, momentum, and energy equations for the micro-region. The effects of wall heat flux and system pressure on the microlayer thickness was analyzed in addition to the its evolution with time before the bubble dry spot appears. The model was applied to the cases of high pressure boiling water into steam, which is particularly relevant to the nuclear industry.

2. GOVERNING EQUATIONS

To model this micro-region, a control volume analysis around the microlayer thickness, δ, was performed. Interfacial shear stress at the liquid-vapor interface was assumed to be negligible. The equation of mass conservation in the microlayer is given below [12].

$$\frac{\partial \delta}{\partial t} = v_l - \frac{\dot{q}}{\rho_l h_{fg}} \tag{1}$$

2.1 Steady State Solution for Microlayer Thickness

$\partial \delta / \partial t = 0$ in steady state. In this case, eq. 1 simplifies to:

$$\dot{q} = \rho_l h_{fg} v_l \tag{2}$$

Separate mass conservation, momentum and energy equations are solved for the micro-region. The liquid velocity normal to the vapor-liquid interface, v_l, is obtained from the continuity equation as shown:

$$\frac{1}{r}\frac{\partial(r u_l)}{\partial r} + \frac{\partial v_l}{\partial y} = 0 \quad \implies \quad v_l = -\frac{1}{r}\frac{\partial}{\partial r}\int_0^\delta r u_l \, dy \tag{3}$$

Assuming laminar flow, the momentum equation for the microlayer is defined as:

$$\frac{\partial P_l}{\partial r} = \mu_l \frac{\partial^2 u_l}{\partial y^2} \tag{4}$$

To solve eq. 4, the following boundary conditions were applied.

$$u_l|_{y=0} = 0, \quad \frac{\partial u_l}{\partial y}|_{y=\delta} = 0$$

The solution of the momentum equation is:

$$u_l = -\frac{1}{\mu_l}\frac{\partial P_l}{\partial r}\left(\delta y - \frac{y^2}{2}\right) \tag{5}$$

Substituting eq. 5 into v_l in eq. 3 and then integrating, gives the following.

$$v_l = \frac{1}{\mu_l}\frac{1}{r}\left(r\frac{\partial P_l}{\partial r}\delta^2\frac{\partial \delta}{\partial r} + r\frac{\partial^2 P_l}{\partial r^2}\frac{\delta^3}{3} + \frac{\partial P_l}{\partial r}\frac{\delta^3}{3}\right) \tag{6}$$

Then, v_l in eq. 6 is substituted into eq. 2.

$$\dot{q} = \frac{\rho_l h_{fg}}{\mu_l}\frac{1}{r}\left(r\frac{\partial P_l}{\partial r}\delta^2\frac{\partial \delta}{\partial r} + r\frac{\partial^2 P_l}{\partial r^2}\frac{\delta^3}{3} + \frac{\partial P_l}{\partial r}\frac{\delta^3}{3}\right) \tag{7}$$

The steady-state energy conservation equation for the thin film is:

$$\dot{q} = \lambda_l\frac{(T_w - T_{int})}{\delta} \quad \implies \quad T_{int} = T_w - \frac{\dot{q}\delta}{\lambda_l} \tag{8}$$

The evaporative heat flux was applied using the modified Clausius Clapeyron equation as [12]:

$$\dot{q} = h_{ev}\left[T_{int} - T_g + \frac{(P_l - P_g)T_g}{\rho_l h_{fg}}\right] \tag{9}$$

T_w is the wall temperature while T_{int} is the temperature at the bubble-microlayer interface. h_{ev} is defined below where R_g is the gas constant of water vapor.

$$h_{ev} = \left(\frac{2}{\pi R_g T_g}\right)^{1/2} \frac{\rho_g h_{fg}^2}{T_g}; \quad T_g = T_{sat}(P_g) \tag{10}$$

The pressures in the vapor and liquid phases satisfy the following relation:

$$P_l = P_g - \sigma\kappa - \frac{A}{\delta^3} + \frac{\dot{q}^2}{\rho_g h_{fg}{}^2} \tag{11}$$

where the dispersion or Hamaker constant, A is 10^{-20}J [12]. The 2nd term on the right hand side in eq. 11 represents the capillary pressure, the 3rd term is the disjoining pressure, while the 4th term accounts for the recoil pressure. κ is the interface curvature with surface tension σ. Substituting P_l in eq. 11 into eq. 9 gives:

$$\dot{q} = h_{ev}\left[T_{int} - T_g + \frac{T_g}{\rho_l h_{fg}}\left(-\sigma\kappa - \frac{A}{\delta^3} + \frac{\dot{q}^2}{\rho_g h_{fg}{}^2}\right)\right] \tag{12}$$

T_{int} in eq. 8 is substituted into eq. 12, which is then equated with $\dot{q}$ in eq. 7. This results in the following:

$$\frac{\partial^2 P_l}{\partial r^2}\frac{\delta^3}{3} + \frac{\partial P_l}{\partial r}\left(\delta^2\frac{\partial\delta}{\partial r} + \frac{\delta^3}{3r}\right) + \frac{\mu_l h_{ev} T_g \sigma}{\rho_l{}^2 h_{fg}{}^2}\kappa = \frac{\mu_l h_{ev}}{\rho_l h_{fg}}\left[T_w - T_g - \frac{\dot{q}\delta}{\lambda_l} + \frac{T_g}{\rho_l h_{fg}}\left(-\frac{A}{\delta^3} + \frac{\dot{q}^2}{\rho_g h_{fg}{}^2}\right)\right] \tag{13}$$

The P_l terms in eq. 11 can be expanded as:

$$\frac{\partial P_l}{\partial r} = -\sigma\frac{\partial\kappa}{\partial r} + \frac{3A}{\delta^4}\frac{\partial\delta}{\partial r} \tag{14}$$

$$\frac{\partial^2 P_l}{\partial r^2} = -\sigma\frac{\partial^2\kappa}{\partial r^2} + \frac{3A}{\delta^4}\frac{\partial^2\delta}{\partial r^2} - \frac{12A}{\delta^5}\left(\frac{\partial\delta}{\partial r}\right)^2 \tag{15}$$

Eqs. 14 & 15 are then substituted into eq. 13. Denoting $\prime$ as $\partial/\partial r$, the resulting rearranged equation is:

$$\begin{aligned}
\kappa'' + \left(\frac{3\delta'}{\delta} + \frac{1}{r}\right)\kappa' - \frac{3\mu_l h_{ev} T_g}{\rho_l{}^2 h_{fg}{}^2 \delta^3}\kappa &= \frac{9A}{\sigma}\left[\frac{\delta''}{\delta^4} - \frac{4(\delta')^2}{\delta^5} + \frac{\delta'}{\delta^4}\left(\frac{\delta'}{\delta} + \frac{1}{3r}\right)\right] \\
&\quad - \frac{3\mu_l h_{ev}}{\rho_l h_{fg}\sigma\delta^3}\left[T_w - T_g - \frac{\dot{q}\delta}{\lambda_l} + \frac{T_g}{\rho_l h_{fg}}\left(-\frac{A}{\delta^3} + \frac{\dot{q}^2}{\rho_g h_{fg}{}^2}\right)\right]
\end{aligned} \tag{16}$$

The interface curvature, κ is defined as follows [12].

$$\kappa = \frac{1}{r}\frac{\partial}{\partial r}\left[\frac{r\delta'}{\sqrt{1 + (\delta')^2}}\right] \tag{17}$$

Eq. 17 can be further simplified as shown.

$$\kappa = \left(1 + (\delta')^2\right)^{-1/2}\left[\delta'' + \frac{\delta'}{r}\right] - (\delta')^2\delta''\left(1 + (\delta')^2\right)^{-3/2} \tag{18}$$

The 1st and 2nd order differentials of κ are obtained as:

$$\kappa' = \left(1 + (\delta')^2\right)^{-1/2}\left[\delta''' + \frac{\delta''}{r} + \delta'\ln r\right] - \left(1 + (\delta')^2\right)^{-3/2}\left[3\delta'(\delta'')^2 + (\delta')^2\delta''' + (\delta')^2\frac{\delta''}{r}\right]$$
$$+ \left(1 + (\delta')^2\right)^{-5/2} \cdot 3(\delta')^3(\delta'')^2 \tag{19}$$

$$\kappa'' = \left(1 + (\delta')^2\right)^{-1/2}\left[\delta'''' + \frac{\delta'''}{r} + 2\delta''\ln r + \delta'r(\ln r - 1)\right]$$
$$- \left(1 + (\delta')^2\right)^{-3/2}\left[3(\delta'')^3 + 9\delta'\delta''\delta''' + (\delta')^2\delta'''' + 3\delta'\frac{(\delta'')^2}{r} + (\delta')^2\frac{\delta'''}{r} + 2(\delta')^2\delta''\ln r\right] \tag{20}$$
$$+ \left(1 + (\delta')^2\right)^{-5/2}\left[18(\delta')^2(\delta'')^3 + 9(\delta')^3\delta''\delta''' + 3(\delta')^3\frac{(\delta'')^2}{r}\right] - \left(1 + (\delta')^2\right)^{-7/2} \cdot 15(\delta')^4(\delta'')^3$$

The 4th-order nonlinear ODE for microlayer thickness at steady state is then obtained by substituting κ, κ', and κ'' from eqs. $(18 - 20)$ into eq. 16 as given below.

$$\delta'''' = \left[3(\delta'')^3 + 9\delta'\delta''\delta''' + 3\delta'\frac{(\delta'')^2}{r} + (\delta')^2\frac{\delta'''}{r} + 2(\delta')^2\delta''\ln r\right]$$
$$- \left(1 + (\delta')^2\right)\left[\delta'''\left(\frac{3\delta'}{\delta} + \frac{2}{r}\right) + \delta''\left(2\ln r + \frac{3\delta'}{\delta r} + \frac{1}{r^2}\right) + \delta'r(\ln r - 1) + \delta'\ln r\left(\frac{3\delta'}{\delta} + \frac{1}{r}\right)\right]$$
$$+ \left(\frac{3\delta'}{\delta} + \frac{1}{r}\right)\left[3\delta'(\delta'')^2 + (\delta')^2\delta''' + (\delta')^2\frac{\delta''}{r}\right] + \left[\left(1 + (\delta')^2\right)^{-2} \cdot 15(\delta')^4(\delta'')^3\right]$$
$$- \left(1 + (\delta')^2\right)^{-1}\left[18(\delta')^2(\delta'')^3 + 9(\delta')^3\delta''\delta''' + 3(\delta')^3(\delta'')^2\left(\frac{3\delta'}{\delta} + \frac{2}{r}\right)\right] \tag{21}$$
$$+ \frac{3\mu_l h_{ev}T_g}{\rho_l^2 h_{fg}^2\delta^3 r}\left[\left(1 + (\delta')^2\right)(r\delta'' + \delta') - r(\delta')^2\delta''\right]$$
$$+ \frac{9A\left(1 + (\delta')^2\right)^{3/2}}{\sigma\delta^4}\left[\delta'' - \frac{4(\delta')^2}{\delta} + \delta'\left(\frac{\delta'}{\delta} + \frac{1}{3r}\right)\right]$$
$$- \frac{3\mu_l h_{ev}\left(1 + (\delta')^2\right)^{3/2}}{\rho_l h_{fg}\sigma\delta^3}\left[T_w - T_g - \frac{\dot{q}\delta}{\lambda_l} + \frac{T_g}{\rho_l h_{fg}}\left(-\frac{A}{\delta^3} + \frac{\dot{q}^2}{\rho_g h_{fg}^2}\right)\right]$$

2.2 Transient Solution for Microlayer Thickness

The transient behavior of microlayer thickness is then studied as a bubble grows and slides along the wall. Here, the behavior of the microlayer before the dry spot appears is analyzed. The conservation of mass equation in eq. 1 can be re-written as:

$$\dot{q} = \rho_l h_{fg}\left(v_l - \frac{\partial\delta}{\partial t}\right) \tag{22}$$

The unsteady momentum equation is given as:

$$\frac{\partial u_l}{\partial t} = -\frac{1}{\rho_l}\frac{\partial P_l}{\partial r} + \frac{\mu_l}{\rho_l}\frac{\partial^2 u_l}{\partial y^2}$$

(23)

To solve eq. 23, the following initial and boundary conditions were applied.

$$u_r|_{y=0} = 0, \quad \frac{\partial u_r}{\partial y}|_{y=\delta} = 0, \quad u_r(t=0) = 0$$

The solution of the unsteady momentum equation is obtained as:

$$u_l(y,t) = \sum_{n=0}^{\infty} \frac{2}{\mu_l\delta}\frac{\partial P_l}{\partial r}\left(\frac{\delta^2}{2\alpha_n} + \frac{1}{\alpha_n^3}\right)\sin(\alpha_n y)\exp\left(-\frac{\mu_l\alpha_n^2 t}{\rho_l}\right) - \frac{1}{\mu_l}\frac{\partial P_l}{\partial r}\left(\delta y - \frac{y^2}{2}\right)$$

(24)

where α_n is defined as:

$$\alpha_n = \frac{(2n+1)\pi}{2\delta} \quad \text{for} \quad n = 0, 1, 2, 3, \ldots$$

(25)

The unsteady energy equation at the microlayer is shown below.

$$\frac{\rho_l c_{pl}}{\lambda_l}\frac{\partial T_l}{\partial t} = \frac{\partial^2 T_l}{\partial y^2}$$

(26)

The following initial and boundary conditions were applied to the energy equation.

$$\frac{\partial T_l}{\partial y}|_{y=0} = -\frac{\dot{q}}{\lambda_l}, \quad \frac{\partial T_l}{\partial y}|_{y=\delta} = 0, \quad T_l(t=0) = T_w$$

The solution for the unsteady energy equation gives:

$$T_l(y,t) = \sum_{m=0}^{\infty} \frac{\dot{q}}{\lambda_l\beta_m^2}\left[(-1)^m - 1\right]\cos(\beta_m y)\exp\left(-\frac{\lambda_l\beta_m^2 t}{\rho_l c_{pl}}\right) - \frac{\dot{q}y}{\lambda_l} + T_w$$
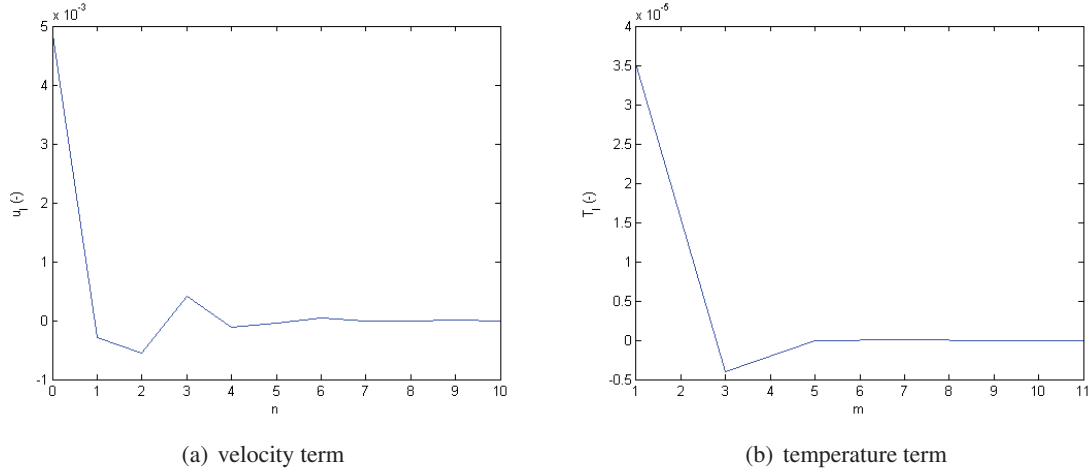
(27)

where β_m is given below.

$$\beta_m = \frac{m\pi}{\delta} \quad \text{for} \quad m = 1, 3, 5, \ldots \quad \text{while} \quad T_l(y,t) = 0 \quad \text{elsewhere}$$

(28)

The rate of convergence of the transient terms in eqs. 24 & 27 is tested in Fig. 2. The plots indicate that each solution converges fast and can be truncated after the 2nd term (n = 1 & m = 3). Thus, the solution for the velocity and temperature profile is approximated by considering the 1st two terms in the series for the transient terms.

Using $n = 0$ & $n = 1$ in eq. 24, the velocity at the microlayer is:

$$u_l(y,t) = -\frac{1}{\mu_l}\frac{\partial P_l}{\partial r}\left(\delta y - \frac{y^2}{2}\right)$$

$$+\frac{\partial P_l}{\partial r}\frac{2\delta^2}{\mu_l\pi}\left[\left(1 + \frac{8}{\pi^2}\right)\sin\left(\frac{\pi y}{2\delta}\right)\exp\left(-\frac{\mu_l\pi^2 t}{4\rho_l\delta^2}\right) + \left(\frac{1}{3} + \frac{8}{27\pi^2}\right)\sin\left(\frac{3\pi y}{2\delta}\right)\exp\left(-\frac{9\mu_l\pi^2 t}{4\rho_l\delta^2}\right)\right]$$

(29)

<center>(a) velocity term   (b) temperature term</center>

<center>**Figure 2: Plot testing the rate of convergence for the series in the transient terms**</center>

Similarly, the microlayer temperature is obtained when $m = 1$ & $m = 3$ are applied in eq. 27.

$$T_l(y,t) = -\frac{2\dot{q}\delta^2}{\lambda_l\pi^2}\left[\cos\left(\frac{\pi y}{\delta}\right)\exp\left(-\frac{\lambda_l\pi^2 t}{\rho_l c_{pl}\delta^2}\right) + \frac{1}{9}\cos\left(\frac{3\pi y}{\delta}\right)\exp\left(-\frac{9\lambda_l\pi^2 t}{\rho_l c_{pl}\delta^2}\right)\right] - \frac{\dot{q}y}{\lambda_l} + T_w \qquad (30)$$

Substituting eq. 29 into eq. 3 results in the liquid velocity normal to the vapor-liquid interface, v_l as shown.

$$
\begin{aligned}
v_l = & -\frac{2t\delta'}{\rho_l}\frac{\partial P_l}{\partial r}\left[\left(1 + \frac{8}{\pi^2}\right)\exp\left(\frac{-\mu_l\pi^2 t}{4\rho_l\delta^2}\right) + 3\left(\frac{1}{3} + \frac{8}{27\pi^2}\right)\exp\left(\frac{-9\mu_l\pi^2 t}{4\rho_l\delta^2}\right)\right] \\
& -\frac{1}{\mu_l}\left[\frac{\partial^2 P_l}{\partial r^2}\delta^3 + \frac{\partial P_l}{\partial r}\left(3\delta^2\delta' + \frac{\delta^3}{r}\right)\right] \\
& \times\left[\frac{4}{\pi^2}\left(1 + \frac{8}{\pi^2}\right)\exp\left(\frac{-\mu_l\pi^2 t}{4\rho_l\delta^2}\right) + \frac{4}{3\pi^2}\left(\frac{1}{3} + \frac{8}{27\pi^2}\right)\exp\left(\frac{-9\mu_l\pi^2 t}{4\rho_l\delta^2}\right) - \frac{1}{3}\right]
\end{aligned}
\qquad (31)
$$

v_l is then substituted into eq. 22 to obtain the heat transfered at the microlayer.

$$
\begin{aligned}
\dot{q} = & -2t\delta' h_{fg}\frac{\partial P_l}{\partial r}\left[\left(1 + \frac{8}{\pi^2}\right)\exp\left(\frac{-\mu_l\pi^2 t}{4\rho_l\delta^2}\right) + 3\left(\frac{1}{3} + \frac{8}{27\pi^2}\right)\exp\left(\frac{-9\mu_l\pi^2 t}{4\rho_l\delta^2}\right)\right] \\
& -\rho_l h_{fg}\frac{\partial \delta}{\partial t} - \frac{\rho_l h_{fg}}{\mu_l}\left[\frac{\partial^2 P_l}{\partial r^2}\delta^3 + \frac{\partial P_l}{\partial r}\left(3\delta^2\delta' + \frac{\delta^3}{r}\right)\right] \\
& \times\left[\frac{4}{\pi^2}\left(1 + \frac{8}{\pi^2}\right)\exp\left(\frac{-\mu_l\pi^2 t}{4\rho_l\delta^2}\right) + \frac{4}{3\pi^2}\left(\frac{1}{3} + \frac{8}{27\pi^2}\right)\exp\left(\frac{-9\mu_l\pi^2 t}{4\rho_l\delta^2}\right) - \frac{1}{3}\right]
\end{aligned}
\qquad (32)
$$

The evaporative heat flux can also be obtained from the modified Clausius Clapeyron equation in eq. 12. However, $T_l(y,t)$ from eq. 30 becomes $T_l(\delta,t)$ as $y \to \delta$, and this replaces T_{int} in eq. 12 to account for the unsteady state.

$$
\begin{aligned}
\dot{q} = & \, h_{ev}\left[T_w - T_g - \frac{\dot{q}\delta}{\lambda_l} + \frac{T_g}{\rho_l h_{fg}}\left(-\sigma\kappa - \frac{A}{\delta^3} + \frac{\dot{q}^2}{\rho_g h_{fg}{}^2}\right)\right] \\
& + \frac{2\dot{q}\delta^2 h_{ev}}{\lambda_l\pi^2}\left[\exp\left(-\frac{\lambda_l\pi^2 t}{\rho_l c_{pl}\delta^2}\right) + \frac{1}{9}\exp\left(-\frac{9\lambda_l\pi^2 t}{\rho_l c_{pl}\delta^2}\right)\right]
\end{aligned}
\qquad (33)
$$

$\dot{q}$ in eqs. 32 & 33 are equated. Then $\partial P_l/\partial r$ and $\partial^2 P_l/\partial r^2$ from eqs. 14 & 15 are substituted. This results in a nonlinear PDE with 4th-order microlayer thickness term and a 1st-order transient term.

$$\frac{\partial \delta}{\partial t} = -\frac{2\dot{q}\delta^2 h_{ev}}{\lambda_l \pi^2 \rho_l h_{fg}}\left[\exp\left(-\frac{\lambda_l \pi^2 t}{\rho_l c_{pl}\delta^2}\right) + \frac{1}{9}\exp\left(-\frac{9\lambda_l \pi^2 t}{\rho_l c_{pl}\delta^2}\right)\right]$$

$$-\frac{h_{ev}}{\rho_l h_{fg}}\left[T_w - T_g - \frac{\dot{q}\delta}{\lambda_l} + \frac{T_g}{\rho_l h_{fg}}\left(-\sigma\kappa - \frac{A}{\delta^3} + \frac{\dot{q}^2}{\rho_g h_{fg}{}^2}\right)\right]$$

$$-\frac{2t\delta'}{\rho_l}\left(-\sigma\kappa' + \frac{3A\delta'}{\delta^4}\right)\left[\left(1 + \frac{8}{\pi^2}\right)\exp\left(\frac{-\mu_l \pi^2 t}{4\rho_l\delta^2}\right) + 3\left(\frac{1}{3} + \frac{8}{27\pi^2}\right)\exp\left(\frac{-9\mu_l \pi^2 t}{4\rho_l\delta^2}\right)\right] \qquad (34)$$

$$-\frac{1}{\mu_l}\left[\delta^3\left(-\sigma\kappa'' + \frac{3A\delta''}{\delta^4} - \frac{12A(\delta')^2}{\delta^5}\right) + \left(-\sigma\kappa' + \frac{3A\delta'}{\delta^4}\right)\left(3\delta^2\delta' + \frac{\delta^3}{r}\right)\right]$$

$$\times\left[\frac{4}{\pi^2}\left(1 + \frac{8}{\pi^2}\right)\exp\left(\frac{-\mu_l \pi^2 t}{4\rho_l\delta^2}\right) + \frac{4}{3\pi^2}\left(\frac{1}{3} + \frac{8}{27\pi^2}\right)\exp\left(\frac{-9\mu_l \pi^2 t}{4\rho_l\delta^2}\right) - \frac{1}{3}\right]$$

where $\kappa(\delta', \delta'')$, $\kappa'(\delta', \delta'', \delta''')$, and $\kappa''(\delta', \delta'', \delta''', \delta'''')$ are defined earlier in eqs. $18-20$.

3.   NUMERICAL PROCEDURE

The numerical analysis of the bubble microlayer was performed in MATLAB. Behavior of the microlayer thickness was studied at different conditions of system pressures ($1-21$ MPa) and wall heat flux ($0.05-2$ MW/m^2). This range covers the nuclear cooling conditions experienced in BWR and PWR. Steam and water were applied as the working fluids. The study was performed using the thermodynamic properties of steam and water [13].

The steady state solution for the 4th-order ODE (eq. 21) was computed using Runge Kutta 4th-order method. To implement this, the 4th-order ODE was decomposed into a system of four 1st-order ODEs. The following boundary conditions were applied where δ_0 is the initial microlayer thickness [12]. $\delta_0 = 10$ μm was applied to maintain a stable solution and avoid singularities. The boundary conditions were obtained by assuming no-slip at the wall and zero gradient at bubble-microlayer interface.

$$\text{At } r = r_0, \quad \delta = \delta_0 \text{ and } \delta' = \delta''' = 0; \quad \text{At } r = r_1, \quad \delta'' = 0$$

Runge-Kutta method requires all the boundary conditions at the start point, but $\delta''(r_0)$ is not known, thus a shooting method was applied using the known boundary condition, $\delta''(r_1) = 0$. Shooting method converts a boundary value problem into a solution of initial value problem. A guess value for $\delta''(r_0)$ was initially applied, and the solution was iterated by shooting for $\delta''(r_1)$. The solution iteration was taken to have converged when $|\delta''(r_1)_{shooting} - \delta''(r_1)| \approx O(10^{-3})$.

The same boundary condition was applied to solve the transient state solution (eq. 34) while the steady state solution was applied as the initial condition. The transient equation with 4th-order ODE and 1st order transient term was decomposed into five 1st-order ODEs. It was then solved using 4th-order Runge Kutta method by marching in time using step size of 10^{-6} for a period of 0.1 μs.

4.   NUMERICAL VALIDATION

The numerical analysis of the bubble microlayer was validated with experimental data from Gao et al. [2] and Koffman & Plesset [14]. Using ethanol as the test fluid at a heat flux of 32.4 kW/m^2 and

atmospheric pressure, the microlayer volume $V(t)$ at time t, before the dry spot appears was computed as follows [2]:

$$V(t) = \int_{r_d}^{R_b} 2\pi r \cdot \delta(r,t) dr \tag{35}$$

$V(t)$ was normalized with microlayer volume at the time the dry spot appeared, $V_d = 0.001166$ mm^3 as shown in Fig. 3. Using eq. 35, the plot depicts a good agreement between the numerical analysis and experimental data.
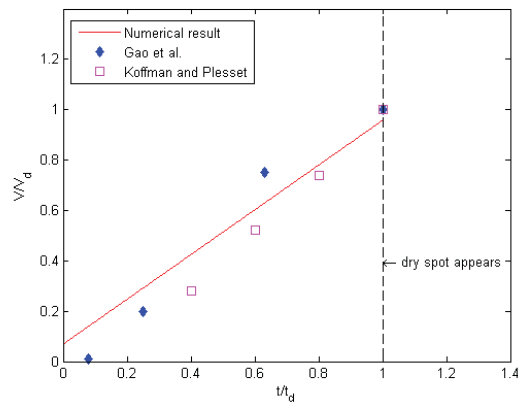

Figure 3: Plot comparing numerical result of normalized microlayer volume with experimental data

At $t = 0$, the microlayer volume is insignificant since the bubble is just nucleated. This result provides confidence in the numerical method applied. It is thus used to study the microlayer behavior at high pressure and high heat flux that cover PWR and BWR operating conditions.

5. RESULTS AND DISCUSSION

Numerical analyses of the behavior at the micro-region was performed for both steady and transient conditions before the bubble dry spot appears. The microlayer thickness, gradient, and interface curvature was studied at different conditions of system pressure and wall heat flux.
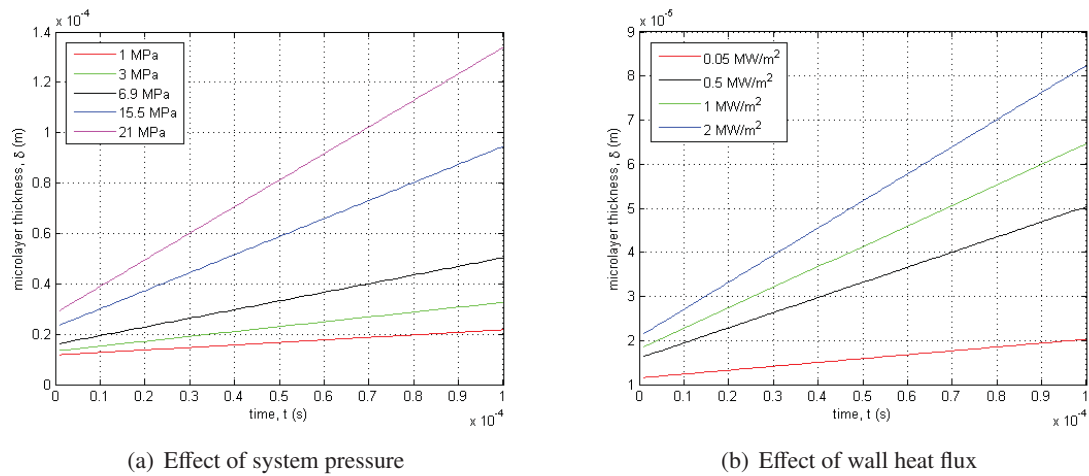
The bubble microlayer thickness increases when the radius of the micro-region was increased as shown in Fig. 4. The microlayer thickness also increases as system pressure was raised between $1 - 21$ MPa, as depicted in Fig. 4(a). This occurs due to the decrease in liquid density as pressure increases. The microlayer thickness under a bubble also increases as the wall heat flux is increases, as given in Fig. 4(b). Thus, higher microlayer thickness indicates that more heat is transferred through the microlayer to the bubble as the wall heat flux is raised.

Behavior of the microlayer transient behavior is given in Fig. 4. It shows that the microlayer thickness increases with time before the dry spot appears. Similar result was obtained by Gao et al. [2]. However, the microlayer thickness would decrease with time after the bubble dry spot appears due to evaporation of the microlayer. The results in heat and mass transfer and subsequent growth of the bubble as the

(a) Effect of system pressure   (b) Effect of wall heat flux
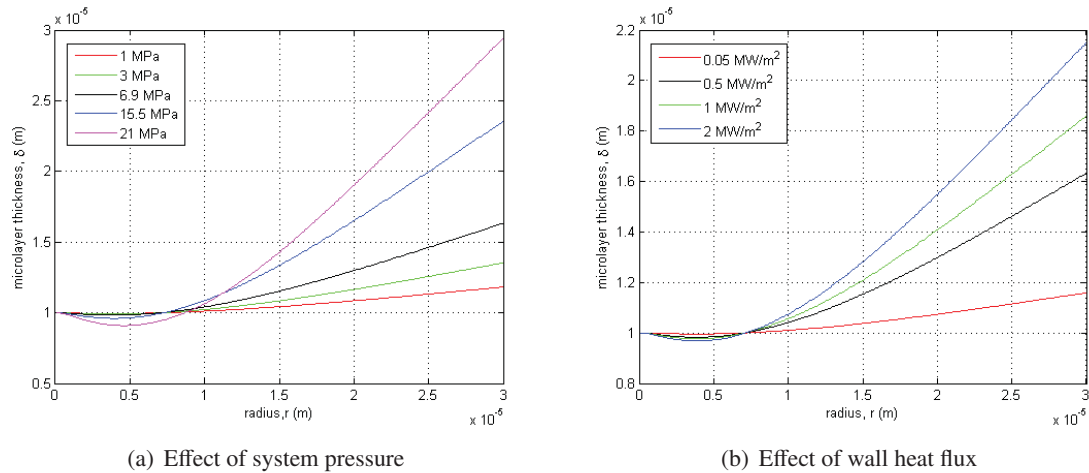
Figure 4: Plot comparing effects of system pressure and wall heat flux on microlayer thickness

microlayer evaporates. Figs. 5(a) & 5(b) also reveals that microlayer thickness increases with system pressure and heat flux as time changes.

(a) Effect of system pressure   (b) Effect of wall heat flux

Figure 5: Plot comparing transient effects of system pressure and wall heat flux on microlayer thickness at $r = 3 \times 10^{-5}$m, before the dry spot appears

Fig. 6 shows the behavior of the microlayer gradient as the stem radius of the bubble was varied. The film gradient increases and reaches a peak as the stem radius increases. The peak gradient is attained faster at higher system pressure and heat flux as shown in Figs. 6(a) & 6(b). The film gradient reveals the magnitude of heat and mass transfer and the contact region between the bubble and the heated wall.

Variation of the interface curvature, κ with the stem radius at the micro-region is given in Fig. 7. The interface curvature affects the pressure gradient and plays a dominant role in the direction of flow over the spreading portion of the contact surface. It also describes the curvature between the bubble and microlayer film. More curvature effect is observed as the system pressure and heat flux was raised. This is due to the decrease in surface tension at higher pressure. Also, a higher degree of curvature is experienced closer to the triple contact point as the stem radius, $r \to 0$ where the bubble comes in direct

(a) Effect of system pressure   (b) Effect of wall heat flux
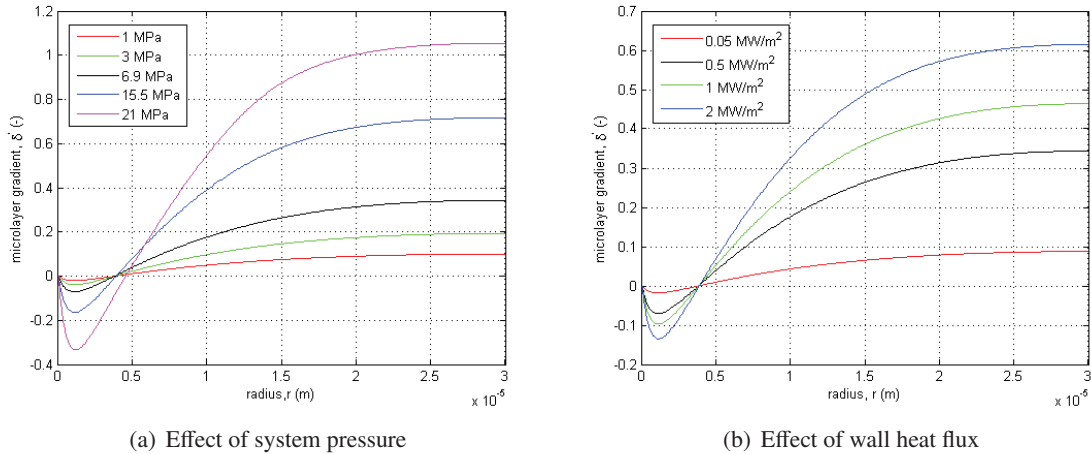
Figure 6: Plot comparing effects of system pressure and wall heat flux on microlayer gradient

contact with the wall.

(a) Effect of system pressure   (b) Effect of wall heat flux
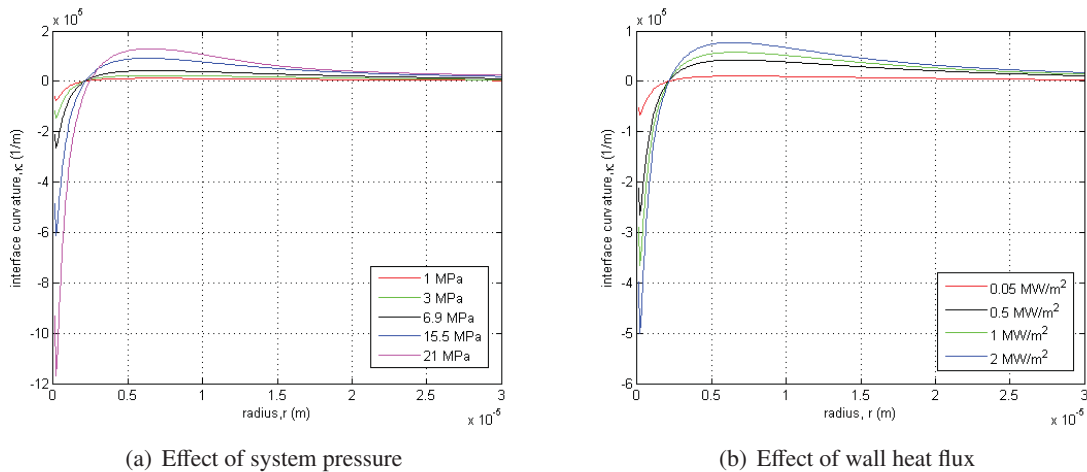
Figure 7: Plot comparing effects of system pressure and wall heat flux on interface curvature

Analysis of the microlayer beneath a growing bubble was performed to improve the prediction of bubble behavior in subcooled boiling. To couple this micro-region model to a bubble growth model, the mass transfer due to the microlayer can be included in the source term of the macro-region equations.

6. CONCLUSIONS

The behavior of the microlayer underneath a bubble during growth was numerically investigated. This was performed at high system pressure and wall heat flux conditions encountered in nuclear reactors. 4th-order equations of the microlayer thickness were derived by combining the mass, momentum, and energy equations at the micro-region. The analysis was done for both steady and unsteady state conditions. The 4th-order Runge Kutta method was employed to compute both equations.

The results indicates that the microlayer thickness increases with the stem radius. The microlayer

thickness also increased with time before the dry spot appears. However, the thickness is expected to diminish with time after the dry spot appears due to evaporation. The result also indicates that microlayer thickness increases with system pressure and wall heat flux. More curvature effect between the bubble and microlayer film was also observed as the system pressure and heat flux increased.

References

1. S. J. D. van Stralen, M. S. Sohal, R. Cole, and W. M. Sluyter, Bubble growth rates in pure and binary systems: Combined effect of relaxation and evaporation microlayers. *Int. J. Heat Mass Transfer*. **Vol. 18**, pp. 453 – 467 (1975).

2. M. Gao, L. Zhang, P. Cheng, and X. Quan, An investigation of microlayer beneath nucleation bubble by laser interferometric method. *Int. J. Heat Mass Transfer*. **Vol. 57**, pp. 183 – 189 (2013).

3. H. H. Jawurek, Simultaneous determination of microlayer geometry and bubble growth in nucleate boiling. *Int. J. Heat Mass Transfer*. **Vol. 12**, pp. 843 – 848 (1969).

4. X. Li, D. K. Hollingsworth, and L. C. Witte, The thickness of the liquid microlayer between a cap-shaped sliding bubble and a heated wall: Experimental measurements. *J. Heat Transfer*. **Vol. 128**, pp. 934 – 944 (2006).

5. Y. Utaka, S. Okuda, and Y. Tasaki, Configuration of the micro-layer and characteristics of heat transfer in a narrow gap mini/micro-channel boiling system. *Int. J. Heat Mass Transfer*. **Vol. 52**, pp. 2205 – 2214 (2009).

6. Y. Utaka, Y. Kashiwabara, and M. Ozaki, Microlayer structure in nucleate boiling of water and ethanol at atmospheric pressure. *Int. J. Heat Mass Transfer*. **Vol. 57**, pp. 222 – 230 (2013).

7. M. G. Cooper and A. J. P. Lloyd, The microlayer in nucleate pool boiling. *Int. J. Heat Mass Transfer*. **Vol. 12**, pp. 895 – 913 (1969).

8. Y. Zhao, T. Masuoka, and T. Tsuruta, Unified theoretical prediction of fully developed nucleate boiling and critical heat flux based on a dynamic microlayer model. *Int. J. Heat Mass Transfer*. **Vol. 45**, pp. 3189 – 3197 (2002).

9. J. H. Lay and V. K. Dhir, Shape of vapor stem during nucleate boiling of saturated liquids. *ASME J. Heat Transfer*. **Vol. 117**, pp. 394 – 401 (1995).

10. G. Son, V. K. Dhir, and N. Ramanujapu, Dynamics and heat transfer associated with a single bubble during nucleate boiling on a horizontal surface. *ASME J. Heat Transfer*. **Vol. 121**, pp. 623 – 631 (1999).

11. D. M. Christopher and L. Zhang, Heat transfer in the microlayer under a bubble during nucleate boiling. *Tsinghua Sci. Tech.*. **Vol. 15**, pp. 404 – 413 (2010).

12. J. Wu and V. J. Dhir, Numerical Simulation of the Dynamics and Heat Transfer Associated With a Single Bubble in Subcooled Pool Boiling. *J. Heat Transfer*. **Vol. 132**, pp. 111501–15 (2010).

13. N. E. Todreas and M. S. Kazimi, *Nuclear Systems I: Thermal Hydraulic Fundamentals*. Taylor & Francis Group, New York (1990).

14. L. D. Koffman and M. S. Plesset, Experimental observations of the microlayer in vapor bubble growth on a heated solid. *J. Heat Transfer*. **Vol. 105**, pp. 625–632 (1983).